Partial Substitution of Cu Sites by Mg for the Improvement of $CuWO_4$ Photoanodes Performance

Sergio González-Poggini[1], Bruno Sánchez[1], Alice Sheppard[2], David J. Fermin[2], Melanie Colet-Lagrille[1*]

[1]Department of Chemical Engineering, Biotechnology and Materials, Faculty of Physical and Mathematical Sciences, Universidad de Chile, Beauchef 851, Santiago, Chile

[2]School of Chemistry, University of Bristol, Cantocks Close, Bristol BS8 1TS, United Kingdom

* corresponding author: mcolet@ing.uchile.cl

Abstract

The photoelectrochemical properties of $CuWO_4$ (Mg x%) thin-films obtained by solution-based methods are investigated as a function of the material composition. The thin-films are prepared by spin-coating a single precursor solution onto FTO-coated glass substrates, followed by an annealing process at 550°C. XRD, Raman, XPS, and electrochemical data studies indicate the formation of single phase $CuWO_4$ (Mg x%), with Mg^{2+} partially substituting Cu^{2+} sites. Photoelectrochemical studies under monochromatic illumination show an 88.2% increase in photocurrent responses and a two-fold increase in charge carriers bulk separation efficiency of 1.0 V vs RHE, upon replacing 2.5% of Cu by Mg. DFT calculations reveal that Mg incorporation rearranges electron density, shifting the position of magnesium towards an axial oxygen atom, increasing the covalent nature of the bond and decreasing the Cu-O bond length. It is proposed that a change in the localization of the electron density away from the sphere of influence of the oxygen atom, and towards the shared space of the covalent bond, leads to better carrier mobility and the generation of higher photocurrents.

Keywords: copper tungstate, photoanode, Mg substitution, DFT calculations, water electrolysis

1. Introduction

In the last decades, continuous industrial development has led to a heavy dependence on fossil fuels, which consumption causes serious consequences for the environment. Among the substitutes to fossil fuels, hydrogen (H_2) features as a viable alternative as it can be used across the energy, heating and transport industries. In this scenario, photoelectrochemical cells (PECs) for H_2 production have emerged as a promising technology since they can promote both light absorption and electrolysis reactions in one device [1].

Numerous metal oxide semiconductors have been investigated as photoanodes for PECs applications. Particularly, semiconductors composed of binary oxides such as ZnO_2, Fe_2O_3 and WO_3 have been widely explored because of their suitable electronic structures to perform the oxygen evolution reaction (OER) [2–4]. However, these materials have shown major drawbacks for their practical implementation, such as remarkably low solar-to-hydrogen (STH) efficiencies, sluggish kinetics towards the OER and poor charge carriers transport properties. Hence, recent research work has focused on developing ternary and multinary metal oxides with the aim of overcoming the limitations of binary oxides. In this sense, ternary oxide semiconductors, such as n-type semiconductors $BiVO_4$, $GaFeO_3$ and $CuWO_4$ have attracted growing attention in recent years as photoanode materials due to their suitable bandgap (2.1 – 2.5 eV) and band edge energy levels for water electrolysis [5–10]. $BiVO_4$ has a theoretical maximum STH efficiency of 9.2%; however, its photoelectrochemical performance is highly limited by low hole-transfer efficiency and poor stability[11]. On the other hand, copper tungstate ($CuWO_4$) has a higher theoretical STH efficiency compared to $BiVO_4$ photoanodes (13%) and has demonstrated to be stable during operation in neutral pH, which makes them a promising alternative for PECs practical implementation [8,12].

$CuWO_4$ crystalizes in a distorted wolframite triclinic structure, which can be described as an arrangement of oxygen atoms in a hexagonal packing, with the cations occupying half of the octahedral sites [13]. Although $CuWO_4$ photoelectrodes have demonstrated a high selectivity towards the OER and stability during operation at neutral pH, their performance is still limited by a substantially low charge carrier separation in the bulk of the photoelectrode, as well as surface recombination at the electrode-electrolyte interphase [8,14]. The band structure of $CuWO_4$ is composed mainly of O 2p states forming the top of the valence band and metal d states forming the minimum of the conduction band. Furthermore,

$CuWO_4$ presents Jahn-Teller effect from the presence of Cu^{2+} $3d^9$ states, which promote distortions on the octahedral CuO_6 clusters [15]. Consequently, the poor charge separation efficiency in the bulk of $CuWO_4$ photoanodes can be strongly influenced by the presence of localized Cu 3d states due to the axial elongation in the CuO_6 octahedra [8,16].

In past years, several strategies have been addressed to tackle the low charge carrier separation in the bulk of $CuWO_4$, such as nanostructuring, heterostructuring or doping [15,17–22]. Alternatively, cation substitution appears as an option that combines the best of these approaches, since using isovalent substitutes and high substitution concentrations can result in substantial changes in the structural, electronic and optical properties of materials [23,24]. In this work, it is described a new facile spin coating synthesis approach using 1:1 water to ethanol solutions to prepare partially magnesium-substituted $CuWO_4$ photoanodes by replacing copper atoms with magnesium in the crystalline structure. It is demonstrated that the obtained magnesium-modified photoanodes exhibit an enhanced bulk charge carrier separation efficiency, and a full characterisation of their composition, electronic structure and photoelectrochemical behaviour is presented.

2. Experimental

2.1. Fabrication of $CuWO_4$ and $CuWO_4$ (Mg x%) photoelectrodes

$CuWO_4$ photoelectrodes were synthesised by spin coating a precursor solution onto 2.5×2.5 cm^2 fluorine-doped tin oxide (FTO) coated glass substrates (surface resistivity 7 Ω/sq, 2.2 mm thickness, Sigma-Aldrich). For the precursor solution preparation, 2 mmol of copper chloride ($CuCl_2 \cdot 2H_2O$, 99.9% purity, Sigma-Aldrich) were dissolved in 1 mL of ultrapure water in a 7 mL glass vial and the solution was stirred in an ultrasonic bath for 15 minutes. Afterwards, 2 mmol of tungsten was added to the solution as ammonium metatungstate (AMT) ($(NH_4)_6H_2W_{12}O_{40} \cdot xH_2O$, 92.0% purity, Sigma-Aldrich) and it was sonicated for 15 minutes. Lastly, 1 mL of ethanol (absolute, Merck) was added to the vial, and the solution was sonicated for 2 hours.

For the synthesis of $CuWO_4$ (Mg x%), nominal copper concentration in the precursor solution was partially replaced by magnesium atoms using magnesium nitrate ($Mg(NO_3)_2 \cdot 6H_2O$, 99.0% purity, Sigma-Aldrich). $CuWO_4$ (Mg x%) photoelectrodes with

nominal atomic concentrations (x values) of 0.01, 0.025 and 0.05 of magnesium were synthesised.

Prior to spin coating, FTO glass substrates were cleaned in an ultrasonic bath following a five-minutes sequence in a solution of 5%v/v Decon 90 surfactant (Decon®), acetone, ultrapure water, and absolute ethanol, subsequently.

The spin coating process was carried out in an automatic pneumatic spin coater (Laurell Technologies Corporation) by dynamic dispensing a 70 µL aliquot of the precursor solution. The spin coating process was performed for 30 seconds using a rotation velocity of 1500 rpm with an acceleration of 3000 rpm s^{-1}. After the deposition of one layer of precursor solution, substrates were placed on a heated plate at 120°C for 3 min, and then cooled down to room temperature before the deposition of an additional layer. The process was repeated until 3 layers were obtained. Finally, the coated substrates were thermally treated in air in a furnace (Carbolite) for 1 hour at 550°C, using a heating/cooling temperature ramp rate of 5°C min^{-1}. A three-layer film was selected as a photoanode based on its average thickness (further information can be found in Section 3.1). Due to the reduced hole diffusion length of $CuWO_4$ (~ 25 nm), the utilization of films with a thickness larger than 600 nm significantly hampers the photoelectrochemical performance of $CuWO_4$ photoelectrodes [25].

2.2. Materials characterisation

The photoelectrodes morphology was characterised by scanning electron microscopy (SEM) employing a Tescan Mira 3 microscope. Elemental analysis was performed through energy-dispersive X-ray spectroscopy (EDS) employing a microscope ZEISS EVO MA10 equipped with a Penta FET Precision Oxford Instrument X-act detector.

Their crystalline structure was analysed by X-ray diffraction (XRD) analysis in a Bruker D8 Advance diffractometer equipped with a CuK_α lamp (α = 0,15406 nm). The diffractograms were collected in the 2θ range between 10 and 50°, using an automatic slit and a scan rate of 0.02° s^{-1}.

The photoelectrodes were also characterised by Raman spectroscopy in a Renishaw RM2000 microscope equipped with a 488 nm Ar laser. The spectra were collected employing a laser intensity of 1% with an exposition time of 60 seconds and were recorded over a wavenumber range from 200 to 1000 cm^{-1}. The surface chemical composition was studied by high-resolution X-ray photoelectron spectroscopy (XPS) at the NanoESCA

facility at the University of Bristol using a non-monochromatic Al Kα X-rays excitation source and an ARGUS spectrometer. Charge correction was performed employing the C 1s peak located at 284.8 eV. The spectra were deconvoluted using a Gaussian-Lorentzian mixture of peak functions and a Shirley background correction. The XPS data analysis was performed using CasaXPS software [26].

The optical bandgap of the electrodes was estimated using Tauc plots constructed from UV-Vis diffuse reflectance spectroscopy (DRS) data. DRS analyses were performed in a PerkinElmer Lambda 650, with a wavelength range from 300 to 800 nm.

2.3. Photoelectrochemical characterisation

The electrochemical and photoelectrochemical characterisations of the photoelectrodes fabricated were performed using a Compactstat potentiostat (IVIUM Technologies). Linear sweep voltammetry (LSV), chronoamperometry (CA) and electrochemical impedance spectroscopy (EIS) in the dark and under illumination conditions were performed. All the experiments were carried out at room temperature (23 ± 1°C), in a glass three electrodes cell equipped with a quartz circular window, using a Pt wire counter electrode and an Ag/AgCl (1 M KCl) reference electrode (Metrohm). The fabricated electrodes were tested as working electrodes and current/photocurrent densities were calculated using the effective geometric area measured using the ImageJ software. The potential against the Ag/AgCl (1 M KCl) reference electrode was converted to the reversible hydrogen electrode (RHE) reference, according to the following expression:

$$E_{RHE} = E_{Ag/AgCl} + 0.059 \cdot pH + 0.197 \quad (1)$$

For photoelectrochemical measurements, a LED monochromatic light (405 nm, Thorlabs) connected to a function generator (SRS DS335, Standford Research Systems) was used as a light source. Light intensity was calibrated using a Si photodiode and an optical power meter (Newport). For the experiments performed under chopped illumination, a square wave with a frequency of 0.05 Hz and a 6 V_{pp} amplitude was used (1.6 mW cm^{-2} light intensity). All experiments were performed in a black metal cage.

Two electrolytes were employed for the photoelectrochemical characterisation of the fabricated electrodes: an aqueous solution composed of 0.1 M Na_2SO_4 in a 0.1 M potassium phosphate (KPi) buffer at pH 7, and an aqueous solution composed of 0.1 M Na_2SO_3 in a 0.1 M KPi buffer at pH 7. Prior to the experiments, electrolytes were purged for 15 min with

Ar. The selected electrolyte composition aligns with previous investigations on $CuWO_4$-based electrodes to ensure comparability, as this specific composition has been employed in prior studies [27–29].

LSV experiments in Na_2SO_4 were recorded over a potential range between 0.6 to 1.5 V vs RHE, with a scan rate of 5 mV s^{-1} and a step size of 1 mV. LSVs measured in Na_2SO_3 were performed over a potential window from 0.6 to 1.1 V vs RHE.

Photocurrent transients were studied by chronoamperometry experiments under chopped illumination. Transient experiments employing Na_2SO_4 as an electrolyte were performed at different applied potentials (0.9, 1.1 and 1.3 V vs RHE) with a sample period of 0.01 s^{-1}. Transient experiments in Na_2SO_3 were recorded at a constant potential of 0.9 V vs RHE.

Mott-Schottky plots were produced from EIS data obtained in the dark over a potential range from 1.2 to 0.4 V vs RHE at 100 Hz, with an AC amplitude of 10 mV.

2.4. Density-functional theory (DFT) computational modelling

In accordance with a study previously reported for a similar photoelectrochemical system [21], DFT computational calculations were performed using the CASTEP package [30–32]. The variable cell geometry optimizations of both the pure and magnesium-substituted $CuWO_4$ structure were calculated using the Perdew-Burke-Ernzerhof functional (PBE) with a Hubbard U correction of 4 eV[33] for the d electrons of the copper atom at a cut-off energy of 1100 eV, while the size of the MP k-point grid was 7×6×7 for the pure $CuWO_4$ and 4×4×4 for the magnesium-substituted supercell. The supercell was constructed by extending two of the cell parameters to obtain a 1×2×2 supercell. pDOS plots were calculated at the same level of theory and analysed through the OptaDOS postprocessing tool. Charge density and electron localization functions were calculated on the optimized structures using CASTEP and extracted using the c2x postprocessing utility.

3. Results and Discussion

3.1. Materials characterisation

Pristine $CuWO_4$ and $CuWO_4$ (Mg x%) films were synthesised by spin coating a precursor solution onto FTO glass substrates, with nominal x values equal to 0.01, 0.025 and 0.05.

The films show as a yellow and translucid porous layer, as expected for triclinic $CuWO_4$ films (see Figure S1) [8,29]. SEM images of the synthesised films are shown in Figure 1. Pure $CuWO_4$ films display a morphology composed of interconnected ovoid crystallites, similar to that reported for $CuWO_4$ films produced by spray pyrolysis [8]. The incorporation of magnesium promotes an alteration in morphology, as a heterogeneous distribution of crystallite sizes is obtained for the $CuWO_4$ (Mg 1.0%), $CuWO_4$ (Mg 2.5%) and $CuWO_4$ (Mg 5.0%) films (Figure 1b−d). The films presented an average thickness ranging from 550 to 650 nm, regardless of the magnesium concentration (Figure S2). Furthermore, Figure S3 presents the EDS elemental analysis of the $CuWO_4$ and $CuWO_4$ (Mg 5.0%) films, revealing a Cu to W ratio of 1.03:1.00 for the $CuWO_4$ film (Figure S3a), aligning well with the expected composition of $CuWO_4$. In Figure S3b, the presence of magnesium in the sample is evidenced; however, quantifying such a small fraction of magnesium through this technique proved challenging due to the overlap of magnesium X-ray peaks with those of copper and tungsten [34].

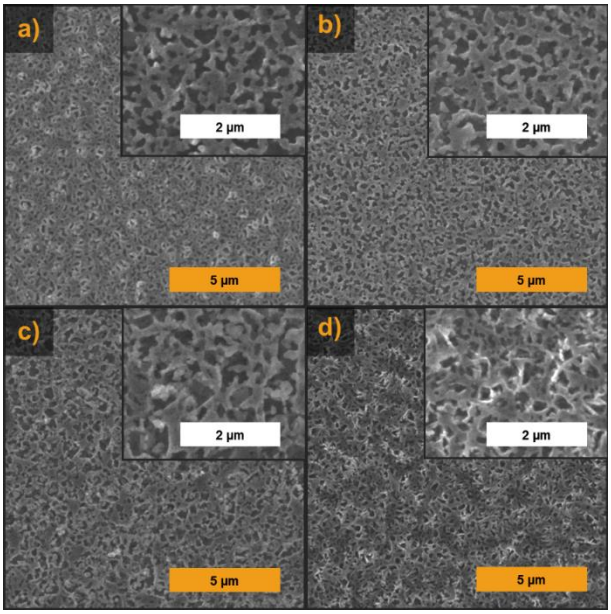

Figure 1. SEM images (5000x) of: a) $CuWO_4$, b) $CuWO_4$ (Mg 1.0%), c) $CuWO_4$ (Mg 2.5%) and d) $CuWO_4$ (Mg 5.0%) films.

The films crystalline phase composition was studied by XRD and Raman spectroscopy. Figure 2 shows the XRD patterns obtained for the films, which are in accordance with the patterns reported for triclinic $CuWO_4$. From the relative intensity of the Bragg reflection planes, it can be noted that the diffractograms obtained for the films display a preferred orientation associated with the (1 0 0) plane, which is comparable to the pattern obtained

for $CuWO_4$ films synthesised by electrodeposition and hydrothermal routes [19,27]. The recorded XRD patterns matched the #2101692 $CuWO_4$ card from the Crystallography Open Database (COD) [35]. Peaks from the FTO glass substrate were also identified which are analogous to those reported for SnO_2 cassiterite (COD #1526637). The diffractograms do not show any sign of WO_3, usually depicted as a shoulder at 2θ = 24.1° [36].

As can be seen in Figure 2, no additional peaks were recorded when incorporating magnesium into the crystalline structure, and no significant change in peak positions was found, which indicates that no significant changes in the interplanar spacing are produced. This could be ascribed to the similarity in ionic radius of Mg^{2+} (0.72 Å) and Cu^{2+} (0.73 Å) cations [37], and the absence of charge compensation [38], which could lead to only small perturbations in the crystalline structure when partially substituting copper atoms with magnesium.

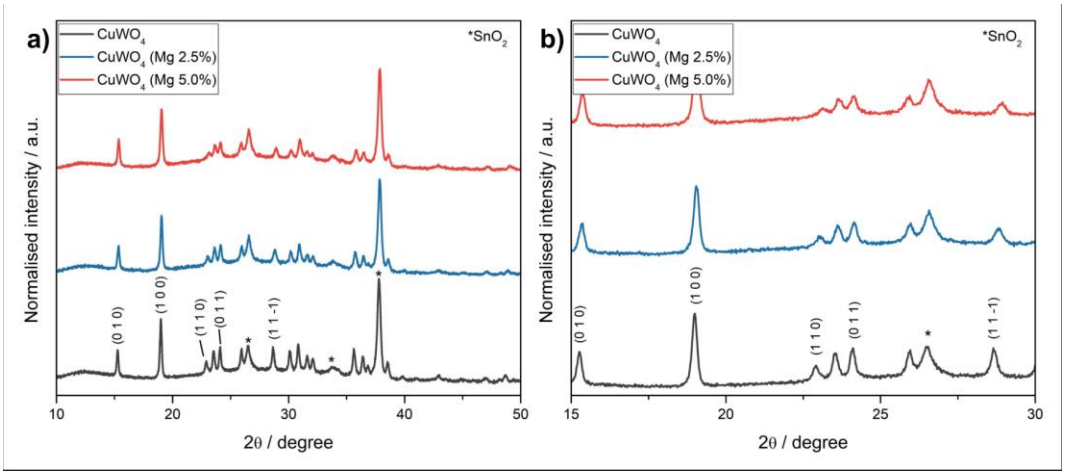

Figure 2. a) XRD patterns of $CuWO_4$, $CuWO_4$ (Mg 2.5%) and $CuWO_4$ (Mg 5.0%) films, b) magnification of diffractograms in the 15–30° range.

To further examine the effect of incorporating magnesium into the structure of $CuWO_4$, a variable cell optimization was performed with finite basis correction. The effect of adding Mg was simulated using a supercell approach where a unitary cell was expanded along two of the axes (a y b) to produce the structure $CuWO_4$ (Mg 12.5%). The resultant crystal cells are presented in Figure S4. As expected, the lattice constants (a, b and c) do not change significantly when replacing a copper site with a magnesium site (< 0.3%), which is in line with the absence of peak displacements discussed before for the XRD analyses. The photoelectrodes average crystallite size was determined by applying the Scherrer equation to the peaks related to the $CuWO_4$ unit cell, and a shape factor of 0.89 (consistent with prior

usage for $CuWO_4$ films [39]) was employed in the calculation. The average crystallite size was 55.8, 41.8 and 51.7 nm for the $CuWO_4$, $CuWO_4$ (Mg 2.5%) and $CuWO_4$ (Mg 5.0%) films, respectively. These values are similar to those previously reported for $CuWO_4$ photoelectrodes (40.0 and 55.3 nm) [39,40].

In the $CuWO_4$ XRD spectrum, the (0 1 0) and (1 0 0) reflection planes are particularly related to the WO_6 octahedra, while the (1 1 0), (0 1 1) and (1 1 -1) planes are predominately associated with the CuO_6 octahedra [41]. A graphic representation of the interception of such planes in the $CuWO_4$ and $CuWO_4$ (Mg 12.5%) crystal structure can be found in Figure S5. A close inspection of Figure 2b suggests that incorporating magnesium mostly alters the CuO_6 octahedra, since no significant changes were observed in the (0 1 0) and (1 0 0) reflection peaks. On the contrary, the peak intensities of the (1 1 0), (0 1 1) and (1 1 -1) planes show a slight reduction when increasing the magnesium content in the film. This change in peak intensity is in good agreement with magnesium substituting copper sites as magnesium has a different electronic structure and X-rays are scattered in proportion to the number of electrons of the atoms composing the crystalline plane [38].

Figure 3 shows the Raman spectra obtained for each photoelectrode, which are in good agreement with patterns reported for the triclinic $CuWO_4$ crystalline structure [15,27]. Similarly to the XRD patterns, no evident shifts in peak position were detected. It can be observed in Figure 3b that the peaks related to O-W-O deformation modes (such as 358 and 398 cm^{-1}) and the A_g W-O band (907 cm^{-1}) do not exhibit significant changes in intensity when incorporating magnesium; however, the A_g mode associated with the CuO_6 octahedra at 292 cm^{-1} displays a noticeable reduction in peak intensity when increasing magnesium content in the film [42]. These results reinforce the initial assumption that magnesium would occupy copper sites in the $CuWO_4$ crystal structure, and they are also in accordance with the XRD patterns and cell optimization results.

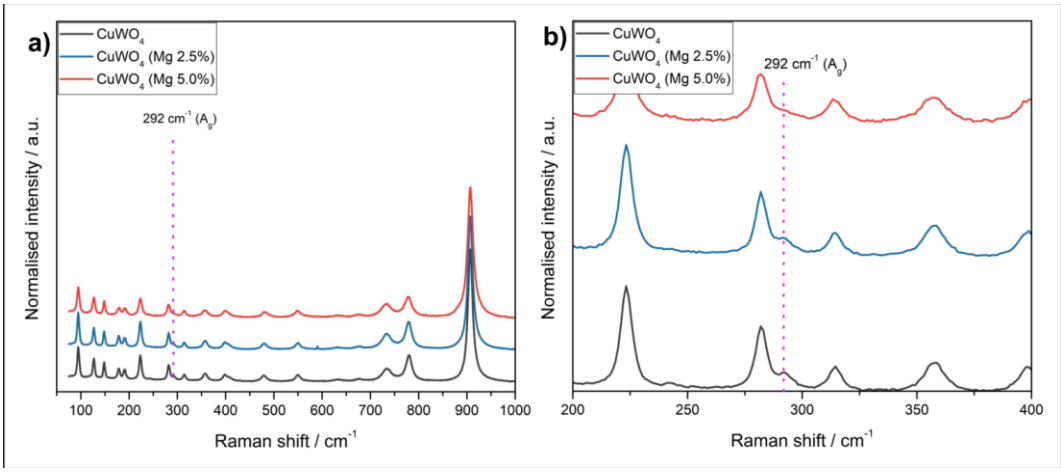

Figure 3. Raman spectra of a) $CuWO_4$, $CuWO_4$ (Mg 2.5%) and $CuWO_4$ (Mg 5.0%) films and b) magnification of the spectra in the 200–400 cm^{-1} range.

A Gaussian–Lorentzian asymmetric fit was used to analyse the XPS spectra and determine the elemental states of Cu, W, O and Mg in the $CuWO_4$ and $CuWO_4$ (Mg 5.0%) films. The XPS spectrum obtained for pristine $CuWO_4$ can be found in Figure S6. Figure 4 shows the XPS spectra obtained for $CuWO_4$ (Mg 5.0%) (additional data on the XPS spectra of $CuWO_4$ (Mg 5.0%) can be found in Figure S7, supporting the presence of magnesium in the sample). The presence of Cu 2p states can be observed in Figure 4a, which are in accordance with Cu(II) species and it exhibits two distinctive Cu(II) satellite collections [43,44]. The doublets associated with Cu $2p_{3/2}$ and Cu $2p_{1/2}$ states exhibit binding energies of 939.2 and 954.5 eV, respectively. The W 4f core-level spectrum (Figure 4b) displays a well-resolved W $4f_{7/2}$ (35.16 eV) and W $4f_{5/2}$ (37.31 eV) doublet, which is consistent with the W^{6+} oxidation state [45]. The fitting of the O 1s peak (Figure 4c) was performed by deconvoluting two peaks located at 530.3 and 531.5 eV, which are typical binding energies for oxygen-metal bonds and adsorbed oxygen, respectively [46]. These results are consistent with previously reported data for $CuWO_4$ films [17–19].

Regarding the incorporation of magnesium, it can be verified from Figure 4d the presence of a peak associated with Mg 1s with a binding energy of 1304 eV, which demonstrates the presence of Mg (II) in the film [47,48].

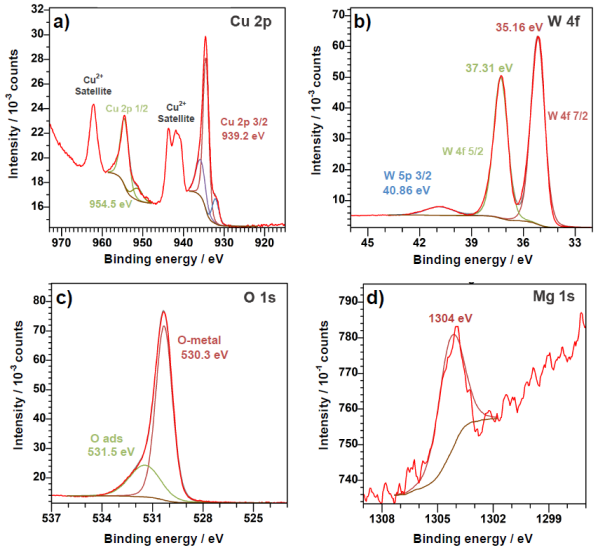

Figure 4. Chemical composition analysis of $CuWO_4$ (Mg 5.0%) photoelectrodes by XPS: a) Cu 2p, b) W 4f, c) O 1s, and d) Mg 1s spectrum.

The optical bandgap of the films was determined by Tauc plots employing DRS data (Figure 5). Tauc plots were constructed assuming an indirect optical transition and the Kubelka-Munk function using the following equation [8,49]:

$$(F(R)\cdot h\nu)^{1/2} = B(h\nu - E_g) \tag{2}$$

where *h* is the Planck constant, *v* is the photon frequency, *B* is a constant of proportionality, E_g is the optical indirect band gap energy, and F(R) is given by [50]:

$$F(R) = \frac{(1-R)^2}{2R} \tag{3}$$

where R is taken to be equal to the ratio R_{sample} / R_{BaSO_4}. From the plots, an optical bandgap energy of 2.50 eV was obtained for the pure $CuWO_4$ film. Similarly, a bandgap of 2.57 and 2.56 eV was obtained for $CuWO_4$ (Mg 2.5%) and $CuWO_4$ (Mg 5.0%) films, respectively. These values are slightly higher than the bandgap reported by other authors (2.30 eV) [8,15]. These higher band gap energies can be attributed to the difference in crystal structure and phase composition obtained in this study since $CuWO_4$ films with similar phase composition and preferred orientation have displayed band gap values of 2.45 and 2.48 eV [27,51]. As the optical band gap energy obtained for the electrodes was practically unaffected by the

incorporation of magnesium, it is possible to assume that magnesium does not significantly affect the band structure of $CuWO_4$.

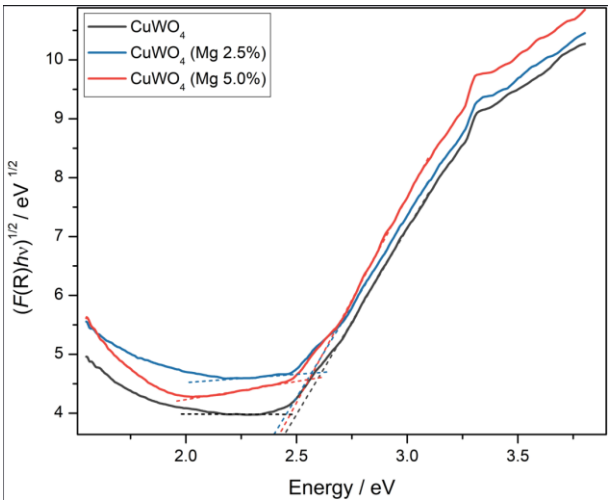

Figure 5. Tauc plots obtained for $CuWO_4$, $CuWO_4$ (Mg 2.5%) and $CuWO_4$ (Mg 5.0%) films.

To further examine this assumption, the electronic structures of both $CuWO_4$ and $CuWO_4$ (Mg 12.5%) optimized cells were simulated using DFT calculations and the partial density of states (pDOS) obtained are shown in Figure 6. A careful analysis of the pDOS data reveals that the valence band of both materials is largely composed of O 2p orbitals and a contribution of Cu 2p states is seen only when getting more deeply into the band. The DOS shows a characteristic first conduction band accessible only to spin down electrons dominated by copper and oxygen orbitals, while a second, broader, conduction band is present for both spin states at a further energy where the tungsten orbitals have a greater contribution. These results are in good agreement with previously reported calculations for $CuWO_4$ [16] at the chosen level of theory (PBE+U) and is a typical band composition for metal oxides, displaying an average bandgap energy of 2.30 eV for the $CuWO_4$ structure [52]. Furthermore, the valence band was also examined by XPS analyses at the beginning of the screening window, which spectra are shown in Figure S8. The obtained spectra are consistent with the pDOS composition, as no significant difference can be observed between the valence band energies of $CuWO_4$ and $CuWO_4$ (Mg 12.5%).

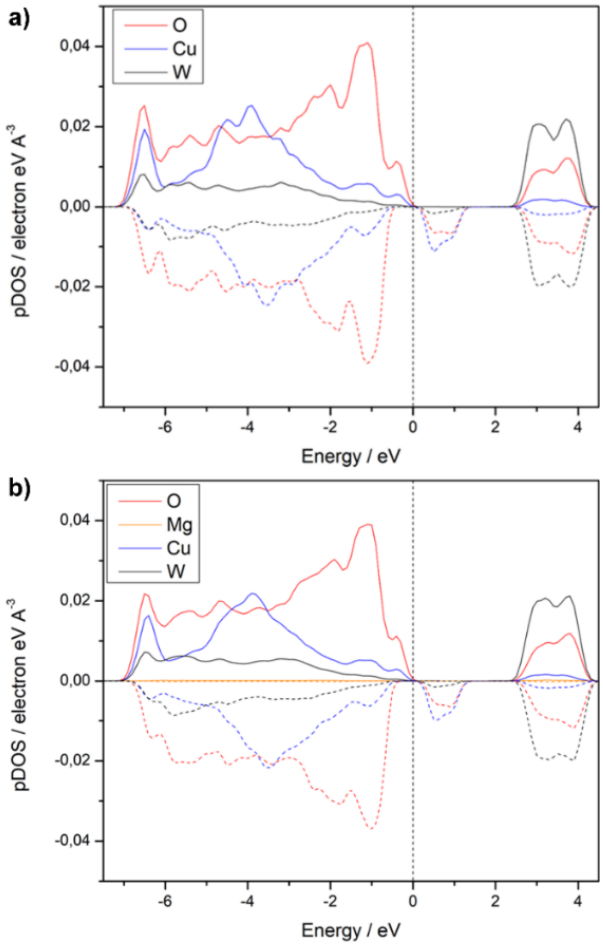

Figure 6. Projected partial density of states (pDOS) of: a) $CuWO_4$ and b) $CuWO_4$ (Mg 12.5%). The DOS was sampled at intervals of 0.1 eV. Full lines represent the spin-up channel and dashed lines represent the spin-down channel. The Fermi level is set to zero for ease of reading.

3.2. Photoelectrochemical behaviour

Figure 7 shows the linear sweep voltammograms obtained for the fabricated photoelectrodes in an electrolyte composed of 0.1 M Na_2SO_4 in 0.1 M Kpi pH 7 under frontal monochromatic chopped illumination (405 nm, 1.6 mW cm^{-2}). In the voltammograms, the n-type behaviour of the photoelectrodes can be verified as an increase in photocurrent density upon illumination. At an applied potential of 1.3 V vs RHE, the $CuWO_4$ photoanodes produce a current density of 18.83 µA cm^{-2}, while the $CuWO_4$ (Mg 1.0%), $CuWO_4$ (Mg 2.5%) and $CuWO_4$ (Mg 5.0%) photoelectrodes exhibited current densities of 25.46 µA cm^{-2}, 35.43 µA cm^{-2} and 27.81 µA cm^{-2}, respectively. It is worth noticing that the increase of magnesium content in the photoelectrode did not generate a monotonic increase in the photocurrent

measured; on the contrary, photocurrent decays when the magnesium atomic content in the photoanode goes from x = 0.025 to x = 0.05. Figure S9 shows the photocurrent onset potential for each photoelectrode under study. It can be noticed that the onset potential scarcely decreases upon increasing the magnesium content in the photoelectrode, with the pristine $CuWO_4$ photoanode exhibiting a photocurrent onset potential of 0.86 V vs RHE and the $CuWO_4$ (Mg 2.5%) photoanode an onset potential of 0.82 V vs RHE. Even though the magnitude of the onset potential change is not significant, the sequence of the change follows the same tendency as the photocurrent density, with the $CuWO_4$ (Mg 2.5%) photoanode exhibiting the lowest onset potential and the higher photocurrent density.

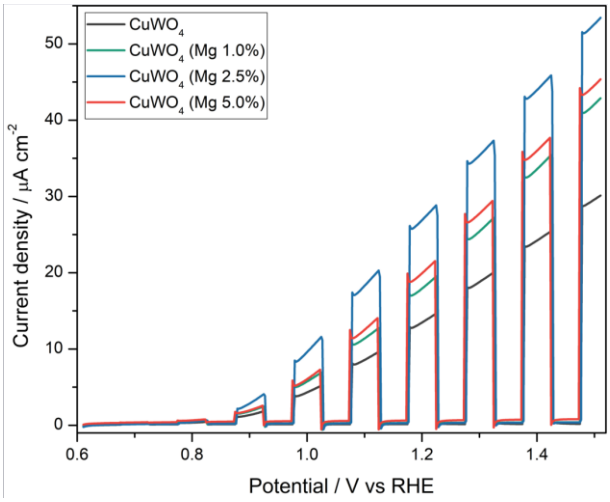

Figure 7. Linear sweep voltammograms obtained in 0.1 M Na_2SO_4 under chopped frontal illumination (405 nm) for the fabricated photoelectrodes (recorded at 5 mV s^{-1}).

The density of donor states and the flat band potentials of the fabricated photoelectrodes were calculated from Mott-Schottky plots (Figure 8), constructed from EIS data obtained in dark conditions at 100 Hz. Table 1 shows the fitted parameters obtained for each electrode using the Mott-Schottky relation:

$$\frac{1}{C_{SC}^2} = \frac{2}{A^2 \varepsilon_0 \varepsilon N_D e}\left(E - E_{FB} - \frac{kT}{e}\right) \quad (4)$$

were C_{SC} is the capacitance of the space charge region, E is the applied potential, E_{FB} is the flat band potential, k is the Boltzmann constant, T is the temperature, *e* is the electron charge, A is the electrode area, ε_0 is the permittivity in vacuum, ε is the permittivity of $CuWO_4$ (ε =83) [18], and N_D is the density of donor states.

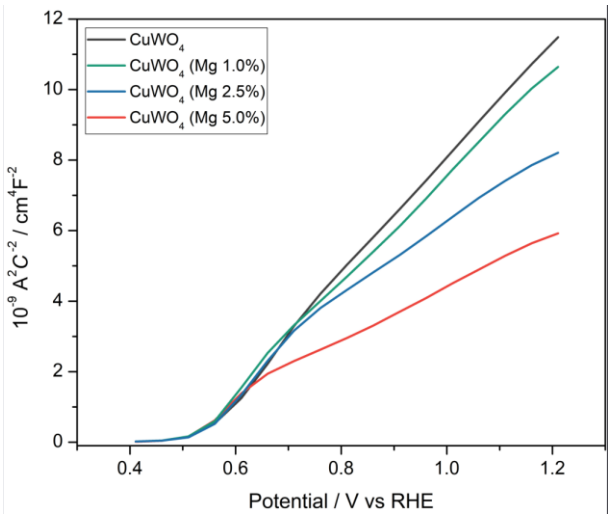

Figure 8. Mott-Schottky plots obtained in 0.1 M Na_2SO_4 for the fabricated photoelectrodes.

Table 1. Flat band potential and donor density fitted from Mott-Schottky plots.

Electrode	E_{FB} / V vs RHE	N_D / cm^{-3}
$CuWO_4$	0.503	$1.04 \cdot 10^{20}$
$CuWO_4$ (Mg 1.0%)	0.500	$1.12 \cdot 10^{20}$
$CuWO_4$ (Mg 2.5%)	0.391	$1.65 \cdot 10^{20}$
$CuWO_4$ (Mg 5.0%)	0.418	$2.25 \cdot 10^{20}$

The flat band potential obtained for the $CuWO_4$ photoelectrodes is similar to those reported in the literature under similar experimental conditions [28,53]. From Table 1, it can be observed that upon the addition of magnesium, the density of donor states increases, obtaining a 58.7 and 116.4% increase for the $CuWO_4$ (Mg 2.5%) and $CuWO_4$ (Mg 5.0%) photoelectrodes, respectively. Additionally, a maximum -112 mV displacement of the flat band potential was obtained for the $CuWO_4$ (Mg 2.5%) photoanode. The displacement of the flat band potential to lower values is a typical phenomenon that occurs in n-type semiconductors when the donor states density is increased [54].

With the aim of determining the influence of magnesium on the enhanced photocurrent obtained for the $CuWO_4$ (Mg 2.5%) photoanode, further photoelectrochemical experiments were carried out for the $CuWO_4$ and $CuWO_4$ (Mg 2.5%) photoelectrodes. Figure 9 shows the current density transients at three different applied potentials (0.9 V vs RHE, 1.1 V vs

RHE and 1.3 V vs RHE) obtained in 0.1 M Na_2SO_4 in 0,1 M KPi pH 7 under frontal monochromatic chopped illumination (405 nm). From the transients, it can be observed an increase in the stationary state current density when comparing the $CuWO_4$ photoanode to the $CuWO_4$ (Mg 2.5%) photoelectrode, which is 20.2%, 24.4% and 49.7%, at 0.9, 1.1 and 1.3 V vs RHE, respectively. Additionally, it can be observed a change in the shape of the "light off" spike, being this spike steeper for the $CuWO_4$ (Mg 2.5%) photoanodes. The decay of photocurrent when interrupting illumination is related to the transport of electrons to surface states which contains trapped holes [55]. In this sense, changes in the spike profile as those shown by the $CuWO_4$ (Mg 2.5%) photoanodes can be attributed to changes in the charge carriers transport in the semiconductor.

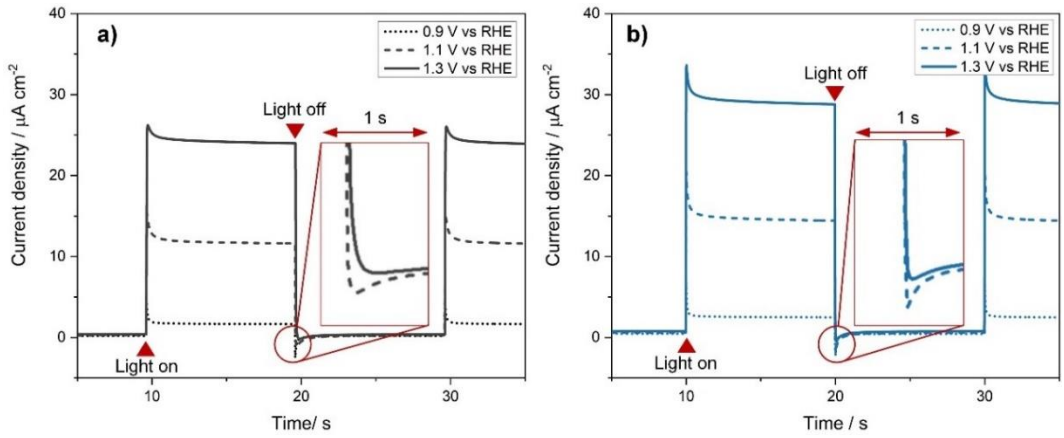

Figure 9. Transient photocurrent responses obtained in 0.1 M Na_2SO_4 at different applied potentials for: a) $CuWO_4$ and b) $CuWO_4$ (Mg 2.5%).

To minimise surface recombination, photocurrent transients were obtained for the $CuWO_4$ and $CuWO_4$ (Mg 2.5%) photoelectrodes in an electrolyte composed of 0.1 M Na_2SO_3. Na_2SO_3 is reported to be an efficient hole scavenger for $CuWO_4$ photoelectrodes, which reduces almost entirely surface recombination at the electrode-electrolyte interphase [56,57]. Figure 10 displays a photocurrent transient obtained at an applied potential of 0.9 V vs RHE. In the presence of Na_2SO_3, the recombination spikes previously shown in Figure 9 disappear as the surface recombination is reduced to a minimum. In this regard, the enhanced photocurrent obtained for the $CuWO_4$ (Mg 2.5%) photoelectrode can be attributed to changes in the bulk charge carriers transport instead of surface phenomena. This behaviour was also verified in linear sweep voltammograms performed under chopped illumination (Figure S10).

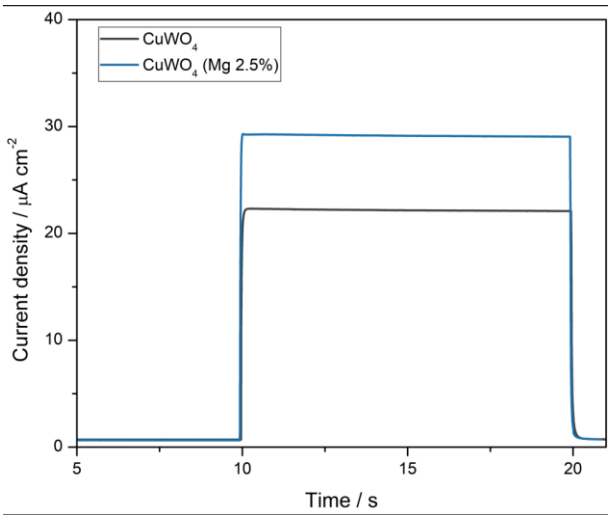

Figure 10. Transient photocurrent responses obtained in 0.1 M Na_2SO_3 at an applied potential of 0.9 V vs RHE for the $CuWO_4$ and $CuWO_4$ (Mg 2.5%) photoelectrodes.

To further study the changes produced by magnesium on the charge carrier transport, the charge density distribution and electron localization function (ELF) of pure $CuWO_4$ and $CuWO_4$ (Mg 12.5%) were calculated from DFT calculations and are shown in Figure S11 and Figure 11, respectively. Figure 11 shows the ELF calculated for both $CuWO_4$ and $CuWO_4$ (Mg 12.5%) structures, through a plane intercepting the axial oxygens of the octahedral and the central atom (copper or magnesium in either case). In the map, warmer colours imply a higher localization of electrons. From Figure 11, it can be observed that for $CuWO_4$, electrons are mostly localized around the oxygen atoms, which implies a higher ionicity of the Cu-O bond. On the other hand, ELF mapping for the $CuWO_4$ (Mg 12.5%) structure shows a higher localization of electrons in the interatomic space. In metal oxide semiconductors, bond character is highly polar due to the high electronegativity of oxygen [52], which implies that electrons are either partially or completely transferred from the metal ion to the more electronegative oxygen, with the electronic transitions occurring predominantly between O 2p and metal d states. This electronic structure can also be verified for $CuWO_4$ and it is illustrated in the pDOS (Figure 6) as the valence band is mainly composed of O 2p states, whereas the conduction band is composed of Cu 3d states. A Mülliken population analysis reveals that one of the axial Mg-O bonds on the magnesium-substituted structure has a shorter length (0.211 nm) and higher population (0.22) than the corresponding Cu-O bond of both the pure $CuWO_4$ structure (0.265 nm and 0.11 respectively) and the adjacent Cu sites (0.256 nm and 0.11 respectively) in the supercell. While most of the Cu-O bonds have a higher ionicity characteristic that remains unchanged

in the substituted structure, the strain introduced by the magnesium doping rearranges the electron density enough to move the position of magnesium towards an oxygen atom, increasing the covalent nature of the bond and decreasing the bond length of the axial oxygen to a length like one of the planar oxygens in the octahedra. In this regard, it is proposed that a change in the localization of the electron density away from the sphere of influence of the oxygen atom and towards the shared space of the covalent bond leads to better carrier mobility and the generation of higher photocurrent [16].

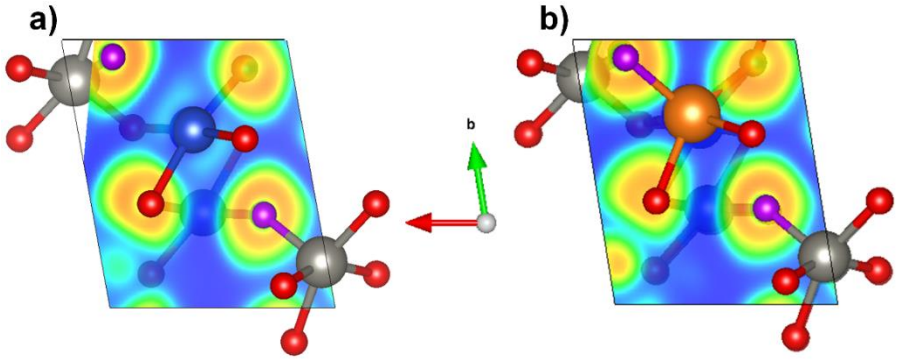

Figure 11. Map of the electron localization function (ELF) calculated for: a) $CuWO_4$ and b) corresponding sites in the supercell for $CuWO_4$ (Mg 12.5%). Blue atoms represent copper, orange atoms represent magnesium, grey atoms represent tungsten, red atoms represent square planar oxygen and purple atoms represent axial oxygen.

Earlier studies report that Cu atoms within $CuWO_4$ display Jahn−Teller distortion in the Cu 3d states, which leads to a strong localization of electrons causing poor carrier transport kinetics and, thus, recombination [8,15]. The difference in the electronic structures of $CuWO_4$ and $CuWO_4$ (Mg x%) arises from the $3d^9$ electrons in Cu singly occupy d_{X2-Y2} orbital, while for magnesium $3s^2$ orbital would not display such a distortion on orbital splitting. Charge density was mapped through three different planes, which maps can be found in Figure S11. The planes were chosen due to the changes in intensity associated with the planes from XRD patterns. Charge density along the (0 1 1) plane shows a decrease in density around the magnesium atom when compared with both the adjacent copper atoms and the corresponding copper atom in the pure structure. The plane (1 1 0) shows a higher charge density around the planar oxygens of the adjacent copper atom. In this sense, highly localized electronic states can act as traps and diminish the electronic conductivity of $CuWO_4$ [58]. These calculations are in accordance with the higher donor density obtained

from Mott-Schottky plots, and a higher electronic conductivity can also explain the higher photocurrent obtained for the $CuWO_4$ (Mg 2.5%) photoanode.

To corroborate this effect, the total photocurrent was analysed in terms of the theoretical photocurrent, the charge transport efficiency in the bulk of the semiconductor, and the surface injection efficiency, as follows [14]:

$$j_{photo} = j_{theoretical} \cdot \eta_{bulk} \cdot \eta_{surface} \quad (5)$$

where j_{photo} is the experimental photocurrent density obtained in a standard electrolyte such as Na_2SO_4, $j_{theoretical}$ is the theoretical photocurrent density resulting from a complete absorption of the incident photon flux, η_{bulk} is the bulk charge carriers transport efficiency, and $\eta_{surface}$ is the surface hole injection efficiency.

In an electrolyte composed of a hole scavenger, such as Na_2SO_3, surface efficiency can be estimated as unity, since Na_2SO_3 has proven to produce quantitative hole collection at the $CuWO_4$ surface[56]. This behaviour is confirmed in Figure 10, as the surface recombination spike is not present in the transients. On the other hand, under monochromatic illumination, the theoretical photocurrent obtained when all photons are absorbed and converted into electron-hole pairs can be estimated as [14]:

$$j_{theoretical} = I_0 \cdot e \quad (6)$$

where I_0 is the experimental photon flux ($3.25 \cdot 10^{25}$ photons cm^{-3}) and e is the electron charge ($1.60 \cdot 10^{-19}$ C). From the photocurrent density obtained in Na_2SO_3 and the stationary current density obtained in Na_2SO_4, bulk and surface efficiencies were calculated for the $CuWO_4$ and $CuWO_4$ (Mg 2.5%) photoelectrodes at several applied potentials, which are shown in Table 2. The calculated efficiencies for pure $CuWO_4$ are similar to those previously reported for $CuWO_4$ [21,59].

Table 2. Bulk and separation efficiencies obtained for the $CuWO_4$ and $CuWO_4$ (Mg 2.5%) photoanodes.

Potential / V vs RHE	$\eta_{bulk}^{CuWO_4}$	$\eta_{surface}^{CuWO_4}$	$\eta_{bulk}^{Mg_{0.025}Cu_{0.975}WO}$	$\eta_{surface}^{Mg_{0.025}Cu_{0.975}WO_4}$
0.7	1%	3%	2%	1%
0.8	3%	3%	5%	2%
0.9	4%	7%	7%	7%
1.0	5%	16%	10%	18%

The surface efficiency of the photoelectrodes slightly increases at high potentials when incorporating magnesium, which may imply that incorporating magnesium modifies $CuWO_4$ surface states or may reduce charge carrier recombination within the space charge region [55]. However, the $CuWO_4$ (Mg 2.5%) photoelectrode exhibits a substantial increase in the bulk efficiency when compared to the $CuWO_4$ photoelectrode, which is in accordance with a better charge carriers transport in the bulk derived from a higher donor density. In the same way, these results are in good agreement with the more delocalized electron distribution obtained in the vicinity of magnesium atoms in the $CuWO_4$ (Mg 12.5%) structure, which increases the electron mobility in the photoelectrode and, hence, reduces bulk recombination of electron-hole pairs.

4. Conclusions

$CuWO_4$ (Mg x%) photoanodes were prepared using a facile spin coating method. Chemical and structural composition analyses indicated the synthesis of triclinic crystalline films with magnesium atoms partially substituting copper sites in the structure. The $CuWO_4$ (Mg 2.5%) photoanodes produced higher photocurrents compared to pristine $CuWO_4$ photoelectrodes upon illumination, exhibiting an 88.2% higher photocurrent density.

DFT calculations were used to study the electronic structure of the synthesised photoelectrodes. The resultant structures showed that for $CuWO_4$ electrons are mostly localized around the oxygen atoms, implying higher ionicity of the Cu-O bond. On the contrary, for the magnesium-modified structure electrons showed a higher localization in the interatomic space.

As previously reported, $CuWO_4$ presents Jahn−Teller distortion of Cu^{2+}, which causes Cu 3d states to be strongly localized. Thus, it is proposed that the electron delocalization induced by the incorporation of magnesium reduces the Jahn-Teller effect and, hence, the electronic conductivity of $CuWO_4$ (Mg x%) photoanodes is increased as a result of better carrier transport kinetic. In this sense, the bulk charge carriers separation efficiency showed a decrease in bulk recombination which is in good agreement with a higher donor density and a higher electronic conductivity induced by magnesium incorporation. This work demonstrates that the partial substitution of Cu^{2+} sites with Mg^{2+} is a good strategy to enhance the charge carriers separation efficiency of $CuWO_4$ based photoelectrodes and improved the overall photocurrent generation during photoelectrochemical water splitting.

Acknowledgments

Melanie Colet-Lagrille, Sergio González-Poggini and Bruno Sánchez are grateful to the financial support by Fondef-ANID Project ID22I10003. Sergio González-Poggini is also grateful to for the Beca Doctorado Nacional-ANID, Ph.D. Scholarship N° 21180182.

Alice Sheppard and David J. Fermin are grateful to the financial support by the Engineering and Physical Sciences Research Council through the SolPV programme (EP/V008676/1). Alice Sheppard is also grateful to for the EPSRC support via the grant EP/T517872/1.

Powered@NLHPC: This research was partially supported by the supercomputing infrastructure of the NLHPC (ECM-02).

Supporting Information Available: Supporting information containing additional experiments and calculations is available free of charge via the Internet at http://pubs.acs.org.

References

(1) Sivula, K.; van de Krol, R. Semiconducting Materials for Photoelectrochemical Energy Conversion. *Nat Rev Mater* **2016**, *1* (2), 15010. https://doi.org/10.1038/natrevmats.2015.10.

(2) Xiao, M.; Luo, B.; Wang, Z.; Wang, S.; Wang, L. Recent Advances of Metal-Oxide Photoanodes: Engineering of Charge Separation and Transportation toward Efficient Solar Water Splitting. *Solar RRL* **2020**, *4* (8), 1900509. https://doi.org/10.1002/solr.201900509.

(3) Wang, J.; van Ree, T.; Wu, Y.; Zhang, P.; Gao, L. Metal Oxide Semiconductors for Solar Water Splitting. In *Metal Oxides in Energy Technologies*; Elsevier, 2018; pp 205–249. https://doi.org/10.1016/B978-0-12-811167-3.00008-0.

(4) Roger, I.; Shipman, M. A.; Symes, M. D. Earth-Abundant Catalysts for Electrochemical and Photoelectrochemical Water Splitting. *Nat Rev Chem* **2017**, *1* (1), 0003. https://doi.org/10.1038/s41570-016-0003.

(5) Chen, D.; Xie, Z.; Tong, Y.; Huang, Y. Review on $BiVO_4$ -Based Photoanodes for Photoelectrochemical Water Oxidation: The Main Influencing Factors. *Energy & Fuels* **2022**, *36* (17), 9932–9949. https://doi.org/10.1021/acs.energyfuels.2c02119.

(6) Lotfi, S.; Ouardi, M. El; Ahsaine, H. A.; Assani, A. Recent Progress on the Synthesis, Morphology and Photocatalytic Dye Degradation of $BiVO_4$ Photocatalysts: A Review. *Catalysis Reviews* **2022**, 1–45. https://doi.org/10.1080/01614940.2022.2057044.

(7) Pilli, S. K.; Deutsch, T. G.; Furtak, T. E.; Brown, L. D.; Turner, J. A.; Herring, A. M. BiVO4/CuWO4 Heterojunction Photoanodes for Efficient Solar Driven Water Oxidation. *Physical Chemistry Chemical Physics* **2013**, *15* (9), 3273. https://doi.org/10.1039/c2cp44577h.

(8) Lhermitte, C. R.; Bartlett, B. M. Advancing the Chemistry of CuWO4 for Photoelectrochemical Water Oxidation. *Acc Chem Res* **2016**, *49* (6), 1121–1129. https://doi.org/10.1021/acs.accounts.6b00045.

(9) Zhang, Z.; Xiao, C.; Li, S. CuWO4 Films Grown via Seeding-Hydrothermal Method for Photoelectrochemical Water Oxidation. *Mater Lett* **2018**, *232*, 25–28. https://doi.org/10.1016/j.matlet.2018.08.075.

(10) Sun, X.; Tiwari, D.; Fermin, D. J. High Interfacial Hole-Transfer Efficiency at $GaFeO_3$ Thin Film Photoanodes. *Adv Energy Mater* **2020**, *10* (45). https://doi.org/10.1002/aenm.202002784.

(11) Zhang, B.; Huang, X.; Zhang, Y.; Lu, G.; Chou, L.; Bi, Y. Unveiling the Activity and Stability Origin of $BiVO_4$ Photoanodes with FeNi Oxyhydroxides for Oxygen Evolution. *Angewandte Chemie International Edition* **2020**, *59* (43), 18990–18995. https://doi.org/10.1002/anie.202008198.

(12) Jian, J.; Jiang, G.; van de Krol, R.; Wei, B.; Wang, H. Recent Advances in Rational Engineering of Multinary Semiconductors for Photoelectrochemical Hydrogen Generation. *Nano Energy* **2018**, *51* (4), 457–480. https://doi.org/10.1016/j.nanoen.2018.06.074.

(13) Khyzhun, O. Yu.; Bekenev, V. L.; Solonin, Yu. M. First-Principles Calculations and X-Ray Spectroscopy Studies of the Electronic Structure of CuWO4. *J Alloys Compd* **2009**, *480* (2), 184–189. https://doi.org/10.1016/j.jallcom.2009.01.119.

(14) Lee, D. K.; Lee, D.; Lumley, M. A.; Choi, K.-S. Progress on Ternary Oxide-Based Photoanodes for Use in Photoelectrochemical Cells for Solar Water Splitting. *Chem Soc Rev* **2019**, *48* (7), 2126–2157. https://doi.org/10.1039/C8CS00761F.

(15) Souza, E. L. S.; Sczancoski, J. C.; Nogueira, I. C.; Almeida, M. A. P.; Orlandi, M. O.; Li, M. S.; Luz, R. A. S.; Filho, M. G. R.; Longo, E.; Cavalcante, L. S. Structural Evolution, Growth Mechanism and Photoluminescence Properties of CuWO4 Nanocrystals. *Ultrason Sonochem* **2017**, *38*, 256–270. https://doi.org/10.1016/j.ultsonch.2017.03.007.

(16) Tian, C. M.; Jiang, M.; Tang, D.; Qiao, L.; Xiao, H. Y.; Oropeza, F. E.; Hofmann, J. P.; Hensen, E. J. M.; Tadich, A.; Li, W.; Qi, D. C.; Zhang, K. H. L. Elucidating the Electronic Structure of $CuWO_4$ Thin Films for Enhanced Photoelectrochemical Water Splitting. *J Mater Chem A Mater* **2019**, *7* (19), 11895–11907. https://doi.org/10.1039/C8TA12070F.

(17) Li, C.; Diao, P. Fluorine Doped Copper Tungsten Nanoflakes with Enhanced Charge Separation for Efficient Photoelectrochemical Water Oxidation. *Electrochim Acta* **2020**, *352*, 136471. https://doi.org/10.1016/j.electacta.2020.136471.

(18) Yang, J.; Li, C.; Diao, P. Molybdenum Doped CuWO4 Nanoflake Array Films as an Efficient Photoanode for Solar Water Splitting. *Electrochim Acta* **2019**, *308*, 195–205. https://doi.org/10.1016/j.electacta.2019.04.044.

(19) Li, K.; Zhang, C.; Li, X.; Du, Y.; Yang, P.; Zhu, M. A Nanostructured CuWO4/Mn3O4 with p/n Heterojunction as Photoanode toward Enhanced Water Oxidation. *Catal Today* **2019**, *335*, 173–179. https://doi.org/10.1016/j.cattod.2018.11.003.

(20) Mavrič, T.; Valant, M.; Forster, M.; Cowan, A. J.; Lavrenčič, U.; Emin, S. Design of a Highly Photocatalytically Active ZnO/CuWO 4 Nanocomposite. *J Colloid Interface Sci* **2016**, *483*, 93–101. https://doi.org/10.1016/j.jcis.2016.08.019.

(21) González-Poggini, S.; Sánchez, B.; Colet-Lagrille, M. Enhanced Photoelectrochemical Activity of $CuWO_4$ Photoanode by Yttrium Doping. *J Electrochem Soc* **2023**, *170* (6), 066512. https://doi.org/10.1149/1945-7111/ace004.

(22) Bohra, D.; Smith, W. A. Improved Charge Separation via Fe-Doping of Copper Tungstate Photoanodes. *Physical Chemistry Chemical Physics* **2015**, *17* (15), 9857–9866. https://doi.org/10.1039/C4CP05565A.

(23) Kim, Y.-I.; Seshadri, R. Optical Properties of Cation-Substituted Zinc Oxide. *Inorg Chem* **2008**, *47* (19), 8437–8443. https://doi.org/10.1021/ic800916a.

(24) Wei, S.-H. Overcoming the Doping Bottleneck in Semiconductors. *Comput Mater Sci* **2004**, *30* (3–4), 337–348. https://doi.org/10.1016/j.commatsci.2004.02.024.

(25) Grigioni, I.; Polo, A.; Nomellini, C.; Vigni, L.; Poma, A.; Dozzi, M. V.; Selli, E. Nature of Charge Carrier Recombination in $CuWO_4$ Photoanodes for Photoelectrochemical Water Splitting.

ACS Appl Energy Mater **2023**, *6* (19), 10020–10029. https://doi.org/10.1021/acsaem.3c01608.

(26) Fairley, N.; Fernandez, V.; Richard-Plouet, M.; Guillot-Deudon, C.; Walton, J.; Smith, E.; Flahaut, D.; Greiner, M.; Biesinger, M.; Tougaard, S.; Morgan, D.; Baltrusaitis, J. Systematic and Collaborative Approach to Problem Solving Using X-Ray Photoelectron Spectroscopy. *Applied Surface Science Advances* **2021**, *5*, 100112. https://doi.org/10.1016/j.apsadv.2021.100112.

(27) Lima, A. E. B.; Costa, M. J. S.; Santos, R. S.; Batista, N. C.; Cavalcante, L. S.; Longo, E.; Luz, G. E. Facile Preparation of CuWO4 Porous Films and Their Photoelectrochemical Properties. *Electrochim Acta* **2017**, *256*, 139–145. https://doi.org/10.1016/j.electacta.2017.10.010.

(28) Yourey, J. E.; Bartlett, B. M. Electrochemical Deposition and Photoelectrochemistry of CuWO4, a Promising Photoanode for Water Oxidation. *J Mater Chem* **2011**, *21* (21), 7651. https://doi.org/10.1039/c1jm11259g.

(29) Tang, Y.; Rong, N.; Liu, F.; Chu, M.; Dong, H.; Zhang, Y.; Xiao, P. Enhancement of the Photoelectrochemical Performance of CuWO 4 Films for Water Splitting by Hydrogen Treatment. *Appl Surf Sci* **2016**, *361*, 133–140. https://doi.org/10.1016/j.apsusc.2015.11.129.

(30) Hohenberg, P.; Kohn, W. Inhomogeneous Electron Gas. *Physical Review* **1964**, *136* (3B), B864–B871. https://doi.org/10.1103/PhysRev.136.B864.

(31) Kohn, W.; Sham, L. J. Self-Consistent Equations Including Exchange and Correlation Effects. *Physical Review* **1965**, *140* (4A), A1133–A1138. https://doi.org/10.1103/PhysRev.140.A1133.

(32) Clark, S. J.; Segall, M. D.; Pickard, C. J.; Hasnip, P. J.; Probert, M. I. J.; Refson, K.; Payne, M. C. First Principles Methods Using CASTEP. *Z Kristallogr Cryst Mater* **2005**, *220* (5–6), 567–570. https://doi.org/10.1524/zkri.220.5.567.65075.

(33) Lalić, M. V.; Popović, Z. S.; Vukajlović, F. R. Ab Initio Study of Electronic, Magnetic and Optical Properties of CuWO4 Tungstate. *Comput Mater Sci* **2011**, *50* (3), 1179–1186. https://doi.org/10.1016/j.commatsci.2010.11.018.

(34) Nasrazadani, S.; Hassani, S. Modern Analytical Techniques in Failure Analysis of Aerospace, Chemical, and Oil and Gas Industries. In *Handbook of Materials Failure Analysis with Case Studies from the Oil and Gas Industry*; Elsevier, 2016; pp 39–54. https://doi.org/10.1016/B978-0-08-100117-2.00010-8.

(35) Vaitkus, A.; Merkys, A.; Gražulis, S. Validation of the Crystallography Open Database Using the Crystallographic Information Framework. *J Appl Crystallogr* **2021**, *54* (2), 661–672. https://doi.org/10.1107/S1600576720016532.

(36) Yourey, J. E.; Pyper, K. J.; Kurtz, J. B.; Bartlett, B. M. Chemical Stability of $CuWO_4$ for Photoelectrochemical Water Oxidation. *The Journal of Physical Chemistry C* **2013**, *117* (17), 8708–8718. https://doi.org/10.1021/jp402048b.

(37) Shannon, R. D. Revised Effective Ionic Radii and Systematic Studies of Interatomic Distances in Halides and Chalcogenides. *Acta Crystallographica Section A* **1976**, *32* (5), 751–767. https://doi.org/10.1107/S0567739476001551.

(38) Atkins, P.; Overton, T. *Shriver & Atkins' Inorganic Chemistry*, 5th ed.; OUP Oxford, 2005; Vol. 165.

(39) Askari, N.; Beheshti, M.; Mowla, D.; Farhadian, M. Synthesis of CuWO4/Bi2S3 Z-Scheme Heterojunction with Enhanced Cephalexin Photodegradation. *J Photochem Photobiol A Chem* **2020**, *394*, 112463. https://doi.org/10.1016/j.jphotochem.2020.112463.

(40) Mavrič, T.; Valant, M.; Forster, M.; Cowan, A. J.; Lavrenčič, U.; Emin, S. Design of a Highly Photocatalytically Active ZnO/CuWO 4 Nanocomposite. *J Colloid Interface Sci* **2016**, *483*, 93–101. https://doi.org/10.1016/j.jcis.2016.08.019.

(41) Ma, L.; Su, J.; Liu, M.; Zhang, L.; Li, Y.; Guo, L. Enhanced Photocatalytic Activity over a Novel $CuWO_4$ /$Cu_{1-x}Zn_xWO_4$ /$ZnWO_4$ Hybrid Material with Sandwiched Heterojunction. *J Mater Res* **2016**, *31* (11), 1616–1621. https://doi.org/10.1557/jmr.2016.114.

(42) Polyakov, B.; Kuzmin, A.; Vlassov, S.; Butanovs, E.; Zideluns, J.; Butikova, J.; Kalendarev, R.; Zubkins, M. A Comparative Study of Heterostructured CuO/CuWO4 Nanowires and Thin Films. *J Cryst Growth* **2017**, *480*, 78–84. https://doi.org/10.1016/j.jcrysgro.2017.10.011.

(43) Biesinger, M. C.; Lau, L. W. M.; Gerson, A. R.; Smart, R. St. C. Resolving Surface Chemical States in XPS Analysis of First Row Transition Metals, Oxides and Hydroxides: Sc, Ti, V, Cu and Zn. *Appl Surf Sci* **2010**, *257* (3), 887–898. https://doi.org/10.1016/j.apsusc.2010.07.086.

(44) Biesinger, M. C. Advanced Analysis of Copper X-Ray Photoelectron Spectra. *Surface and Interface Analysis* **2017**, *49* (13), 1325–1334. https://doi.org/10.1002/sia.6239.

(45) Alov, N. V. Determination of the States of Oxidation of Metals in Thin Oxide Films by X-Ray Photoelectron Spectroscopy. *Journal of Analytical Chemistry* **2005**, *60* (5), 431–435. https://doi.org/10.1007/s10809-005-0114-x.

(46) Nohira, H.; Tsai, W.; Besling, W.; Young, E.; Petry, J.; Conard, T.; Vandervorst, W.; De Gendt, S.; Heyns, M.; Maes, J.; Tuominen, M. Characterization of ALCVD-Al2O3 and ZrO2 Layer Using X-Ray Photoelectron Spectroscopy. *J Non Cryst Solids* **2002**, *303* (1), 83–87. https://doi.org/10.1016/S0022-3093(02)00970-5.

(47) Predoi, D.; Ciobanu, C. S.; Iconaru, S. L.; Raaen, S.; Badea, M. L.; Rokosz, K. Physicochemical and Biological Evaluation of Chitosan-Coated Magnesium-Doped Hydroxyapatite Composite Layers Obtained by Vacuum Deposition. *Coatings* **2022**, *12* (5), 702. https://doi.org/10.3390/coatings12050702.

(48) Gholinejad, M.; Bahrami, M.; Nájera, C.; Pullithadathil, B. Magnesium Oxide Supported Bimetallic Pd/Cu Nanoparticles as an Efficient Catalyst for Sonogashira Reaction. *J Catal* **2018**, *363*, 81–91. https://doi.org/10.1016/j.jcat.2018.02.028.

(49) Landi, S.; Segundo, I. R.; Freitas, E.; Vasilevskiy, M.; Carneiro, J.; Tavares, C. J. Use and Misuse of the Kubelka-Munk Function to Obtain the Band Gap Energy from Diffuse

Reflectance Measurements. *Solid State Commun* **2022**, *341*, 114573. https://doi.org/10.1016/j.ssc.2021.114573.

(50) Makuła, P.; Pacia, M.; Macyk, W. How To Correctly Determine the Band Gap Energy of Modified Semiconductor Photocatalysts Based on UV–Vis Spectra. *J Phys Chem Lett* **2018**, *9* (23), 6814–6817. https://doi.org/10.1021/acs.jpclett.8b02892.

(51) Ding, W.; Wu, X.; Lu, Q. Structure and Photocatalytic Activity of Thin-Walled CuWO4 Nanotubes: An Experimental and DFT Study. *Mater Lett* **2019**, *253*, 323–326. https://doi.org/10.1016/j.matlet.2019.06.109.

(52) Krol, R. va de; Grätzel, M. *Photoelectrochemical Hydrogen Production*, 1st ed.; van de Krol, R., Grätzel, M., Eds.; Electronic Materials: Science & Technology; Springer US: Boston, MA, 2012; Vol. 102. https://doi.org/10.1007/978-1-4614-1380-6.

(53) Hill, J. C.; Ping, Y.; Galli, G. A.; Choi, K.-S. Synthesis, Photoelectrochemical Properties, and First Principles Study of n-Type CuW1−xMoxO4 Electrodes Showing Enhanced Visible Light Absorption. *Energy Environ Sci* **2013**, *6* (8), 2440. https://doi.org/10.1039/c3ee40827b.

(54) Norio Sato. *Electrochemistry at Metal and Semiconductor Electrodes*; Elsevier, 1998. https://doi.org/10.1016/B978-0-444-82806-4.X5000-4.

(55) Peter, L. M. Dynamic Aspects of Semiconductor Photoelectrochemistry. *Chem Rev* **1990**, *90* (5), 753–769. https://doi.org/10.1021/cr00103a005.

(56) Gao, Y.; Hamann, T. W. Elucidation of $CuWO_4$ Surface States During Photoelectrochemical Water Oxidation. *J Phys Chem Lett* **2017**, *8* (12), 2700–2704. https://doi.org/10.1021/acs.jpclett.7b00664.

(57) Fermín, D. J.; Ponomarev, E. A.; Peter, L. M. A Kinetic Study of CdS Photocorrosion by Intensity Modulated Photocurrent and Photoelectrochemical Impedance Spectroscopy. *Journal of Electroanalytical Chemistry* **1999**, *473* (1–2), 192–203. https://doi.org/10.1016/S0022-0728(99)00109-6.

(58) Yourey, J. E.; Kurtz, J. B.; Bartlett, B. M. Structure, Optical Properties, and Magnetism of the Full $Zn_{1-x}Cu_xWO_4$ ($0 \leq x \leq 1$) Composition Range. *Inorg Chem* **2012**, *51* (19), 10394–10401. https://doi.org/10.1021/ic301607g.

(59) Wang, D.; Bassi, P.; Qi, H.; Zhao, X.; Gurudayal; Wong, L.; Xu, R.; Sritharan, T.; Chen, Z. Improved Charge Separation in WO3/CuWO4 Composite Photoanodes for Photoelectrochemical Water Oxidation. *Materials* **2016**, *9* (5), 348. https://doi.org/10.3390/ma9050348.